communications biology

A Nature Portfolio journal

Article

https://doi.org/10.1038/s42003-025-07937-9

m^{6}A modification regulates cell proliferation via reprogramming the balance between glycolysis and pentose phosphate pathway

Jian-Fei Xi[1,6], Biao-Di Liu[1,6], Guo-Run Tang[1,6], Ze-Hui Ren[1], Hong-Xuan Chen[1], Ye-Lin Lan[1], Feng Yin[2], Zigang Li[2], Wei-Sheng Cheng[3], Jinkai Wang[3], Lili Chen[4], Shao-Chun Yuan[1], Zhang Zhang[1] & Guan-Zheng Luo[1,2,5]

N6-methyladenosine (m^{6}A) stands as the predominant modification in eukaryotic mRNA and is involved in various biological functions. Aberrant m^{6}A has been implicated in abnormal cellular phenotypes, including defects in stem cell differentiation and tumorigenesis. However, the precise effects of m^{6}A on cell proliferation and the underlining mechanism of metabolic gene regulation remain incompletely understood. Here, we established a cellular environment with low-m^{6}A levels and observed a severe impairment of cell proliferation. Mechanistic studies revealed that the depletion of m^{6}A on TIGAR mRNA led to increased expression, subsequently inhibiting glycolysis while promoting the pentose phosphate pathway (PPP). A genome-wide CRISPR-Cas9 screen identified numerous genes involved in cell proliferation that are sensitive to m^{6}A modification, with G6PD emerging as a key regulator. Integration of gene expression and survival data from cancer patients suggested that patients with elevated G6PD expression may exhibit enhanced responsiveness to tumor growth inhibition through m^{6}A suppression. Our findings elucidate the critical role of m^{6}A in cell proliferation, highlighting the therapeutic potential of targeting m^{6}A-mediated metabolic pathways in cancer.

RNA modification has been recognized as a crucial layer that regulates the RNA life cycle and significantly influences gene expression, thereby affecting various biological processes. Among over 170 types of RNA modifications identified in eukaryotes, N6-methyladenosine (m^{6}A) is one of the most prevalent and abundant type on mRNA[1,2]. Recent work has uncovered the role of m^{6}A in diverse physiological and pathological scenarios[2], spanning embryo development to human diseases such as cancer[3,4]. Due to its indispensable role in cell proliferation, the aberrant expression of the m^{6}A "writer", METTL3, has been reported in a variety of cancer types[5–9]. As an oncogene, METTL3 expression exhibits a notable elevation in lung adenocarcinoma (LUAD) and colon adenocarcinoma, a trend consistently observed across multiple instances in the Cancer Genome Atlas (TCGA) datasets[8]. Correspondingly, a highly potent and selective METTL3 inhibitor, STM2457, has been reported to result in reduced AML growth and an increase in differentiation and apoptosis in vivo[10]. These findings highlight the potential of METTL3 as a new anticancer target. Nevertheless, the underlining mechanisms by which m^{6}A exerts its role in carcinogenesis and downstream gene(s) responsible for these cellular phenotypes remain elusive.

Carcinogenesis represents a specific cellular phenotype wherein cells undergo uncontrolled replication. In order to fulfill the biosynthetic demands associated with proliferation, cancer cells increase the import of nutrients from a frequently nutrient-poor environment[11]. Therefore, cancer cells reprogram cellular metabolism to maintain viability and build new biomass

[1]MOE Key Laboratory of Gene Function and Regulation, Guangdong Province Key Laboratory of Pharmaceutical Functional Genes, State Key Laboratory of Biocontrol, School of Life Sciences, Sun Yat-sen University, Guangzhou, China. [2]Pingshan Translational Medicine Center, Shenzhen Bay Laboratory, Shenzhen, China. [3]Department of Medical Informatics, Zhongshan School of Medicine, Sun Yat-sen University, Guangzhou, China. [4]Guangdong Provincial Key Laboratory of Stomatology, Hospital of Stomatology, Guanghua School of Stomatology, Sun Yat-sen University, Guangzhou, China. [5]Sun Yat-sen University Institute of Advanced Studies Hong Kong, Science Park, Hong Kong SAR, China. [6]These authors contributed equally: Jian-Fei Xi, Biao-Di Liu, Guo-Run Tang. e-mail: luogzh5@mail.sysu.edu.cn

as both direct and indirect consequence of oncogenic mutations. The main pathway of glucose metabolism in cancer cells is aerobic glycolysis, commonly referred to as the Warburg effect[12]. To sustain accelerated cell proliferation, cancer cells necessitate increased uptake of nutrients, augmented flux through biosynthetic pathways, support for metabolic intermediates, and the continuous replenishment of cofactors required for supplying energy or reducing equivalents in cellular reactions[13]. The preference for aerobic glycolysis metabolic pathway generates essential metabolic precursors crucial for the rapid proliferation of cancer cells[14]. However, aerobic glycolysis often accumulates electron transport flux that exceeds the capacity of the ATP synthase, resulting in the formation of excess reactive oxygen species (ROS). Whereas moderate levels of ROS constitute an important signaling input that contributes to the maintenance of the tumorigenic state, overproduction of ROS is detrimental to cell growth and survival[15]. The glycolytic intermediate glucose-6-phosphate can be redirected into the pentose phosphate pathway (PPP), with glucose-6-phosphate dehydrogenase (G6PD) as the rate-limiting enzyme. This process supports the regeneration of reduced NADPH from its oxidized form (NADP +), thereby contributing to cellular defense against oxidative stress[11,16]. In addition, TIGAR, a downstream effector of p53, has been reported to inhibit glycolysis and enhance the flow of the pentose phosphate pathway, resulting in the production of essential nicotinamide adenine dinucleotide phosphate (NADPH) and ribose[17,18]. Therefore, oncogene-driven metabolic reprogramming allows cancer cells to maintain deregulated proliferation. Dissecting the metabolic adaptations that tumors rely on to promote these changes can provide valuable insights for developing novel therapeutic strategies.

Emerging research has highlighted the importance of epigenetic modifications in regulating cancer cell glucose metabolism, including DNA methylation[19,20], histone modifications[20], and non-coding RNAs[21]. Recent studies have demonstrated that the m^{6}A modification significantly impacts cancer cell glucose metabolism[22,23]. Modulating m^{6}A methylation levels can influence the metabolic signaling pathways, transcription factors and glucose metabolism enzymes. For instance, in cervical and liver cancer (LIHC), m^{6}A positively regulates the glycolysis of cancer cells through controlling *PDK4* translation elongation and mRNA stability[24]. In colorectal cancer, the long non-coding RNA *LINRIS* inhibits K139 ubiquitination of the m^{6}A reader IGF2BP2 and stabilizes its expression via the autophagy lysosomal pathway, thereby enhancing c-Myc-mediated glycolysis through the LINRIS-IGF2BP2-c-Myc axis and promoting cancer progression[25]. However, despite the establishment of METTL3 as a potential anticancer target, the consequence of cellular phenotype and relevant metabolic reprogramming following the deficiency of m^{6}A remain unclear.

To explore the potential strategy for cancer therapy through modulation of m^{6}A, we used the METTL3 inhibitor STM2457 to induce a reduction in intracellular m^{6}A levels, allowing for the systematic investigation of the effects of m^{6}A deficiency across multiple cell lines and species. Consistently, we observed inhibited cell proliferation and decreased glucose glycolysis in this model. Furthermore, we found that m^{6}A modification negatively regulates the *TIGAR* gene expression through YTHDF2-mediated RNA degradation. To better understand the underling mechanism driving reprogrammed cell metabolism and impaired cell proliferation under m^{6}A deficiency, we conducted a genome-scale CRISPR-Cas9 genetic screen in a low m^{6}A level environment. This screen identified major component genes of the m^{6}A methyltransferase complex and m^{6}A readers responsible for cell proliferation, as well as previously unrecognized genes whose deletion compensated for the impaired cell proliferation resulting from m^{6}A deficiency. Further study demonstrated that low m^{6}A level decrease ROS levels through the key regulator gene *G6PD*, resulting in CDK2 T160 phosphorylation reduction and S phase arrest. Integration of gene expression and survival data from LIHC patients in TCGA suggests specific subsets with elevated *G6PD* expression may exhibit enhanced responsiveness to METTL3 inhibition therapy. These findings underscore the significance of epitranscriptomic regulation in glucose metabolism pathways, revealing the crucial role of m^{6}A modification in regulating cell proliferation and its potential implications for cancer therapy.

Results

STM2457 effectively reduces m^{6}A levels and impairs cell proliferation

It has been reported that *METTL3* knockout is detrimental for most cells, while certain escaped cell lines exhibit the expression of altered but functional METTL3 isoforms and retained m^{6}A modification[26]. To better understand the indispensability of m^{6}A for cell survival in different cell types, we explored the Cancer Dependency Map Project (DepMap) dataset which measures cell proliferation in 1,054 cell lines following a CRISPR loss-of-function screen, confirming that most cell lines are dependent on *METTL3* (Chronos dependency score <0.5) (Fig. 1A). Therefore, we applied the STM2457, a highly potent and selective catalytic inhibitor of METTL3 to create an intracellular environment with reduced m^{6}A[10]. Mass spectrometry demonstrated that after treatment with 5 μM of STM2457 for an hour, m^{6}A level declined to 74%. Prolonging the exposure or increasing the inhibitor dosage further decreased m^{6}A level (Fig. 1B, Supplementary Fig. 1B).

To confirm the broad efficacy of STM2457, we tested its effect across multiple cell types and species (Supplementary Fig. 1A, B). As expected, based on the high conservation of the METTL3 catalytic domain (Supplementary Fig. 1C), STM2457 consistently reduced m^{6}A levels across a range of biological systems (human, mouse, chicken, and fruit fly) in a concentration- and duration-dependent manner (Supplementary Fig. 1D, E). To further investigate whether this m^{6}A inhibitor has any preference on specific gene, we performed MeRIP-seq assay to determine the m^{6}A alteration patterns in HEK293T cells. Treatment with STM2457 altered m^{6}A levels in 5718 genes, with 5715 showing reduced m^{6}A that accounting for 67.6% of all m^{6}A-modified genes (Supplementary Fig. 1F). This widespread reduction in m^{6}A was relatively uniform across different regions of the transcripts, indicating that STM2457 does not exhibit gene-specific or region-specific biases (Fig. 1C). Thus, STM2457 effectively generates a stable cellular model with globally reduced m^{6}A modification.

We next evaluated the proliferation rates of various human cell lines following STM2457 treatment. Cell counting demonstrated a dose-dependent inhibition of proliferation, with HEK293T and HuH7 cells showing the strongest response, while HeLa cells were less sensitive (Fig. 1D). These results highlighted a consistent cellular response to m^{6}A modification loss among the tested cell lines. Subsequent analyses of the cell cycle and apoptosis in HEK293T cells post-inhibition indicated a notable augmentation in the S phase of the cell cycle compared to control conditions, with no discernible alterations in apoptosis post-treatment (Fig. 1E). These results suggest that STM2457 impacts cell proliferation primarily through cell cycle modulation. To confirm that these effects were mediated by reduced m^{6}A levels, we performed METTL3 knockdown experiments in different cell lines (Supplementary Fig. 2A). Mirroring the effects of STM2457 treatment, METTL3 knockdown significantly inhibited proliferation and induced S phase arrest in HEK293T and HuH7 cells, with less pronounced effects HeLa cells (Supplementary Fig. 2B, C). These results strongly support the conclusion that the observed effects of STM2457 are mediated through METTL3-dependent reduction in m^{6}A levels.

TIGAR is a key target of m^{6}A-mediated regulation of cell proliferation

To investigate the mechanism by which m^{6}A regulates cell proliferation, we performed RNA-seq in HEK293T cells treated with STM2457. We observed significant changes in the expression of numerous genes, with 104 genes upregulated and 84 downregulated (Fig. 2A). GO enrichment analysis of these differentially expressed genes highlighted the oxidative stress response, negative phosphorylation regulation, and the p53 transcriptional gene network (Fig. 2B). Further analysis of MeRIP-seq data revealed that genes with augmented expression possessed a greater number of m^{6}A modification sites relative to those with reduced expression, suggesting a direct effect of m^{6}A to regulation gene expression (Fig. 2C). Intriguingly, gene expression variances showed an inverse relationship with m^{6}A alterations, consistent to

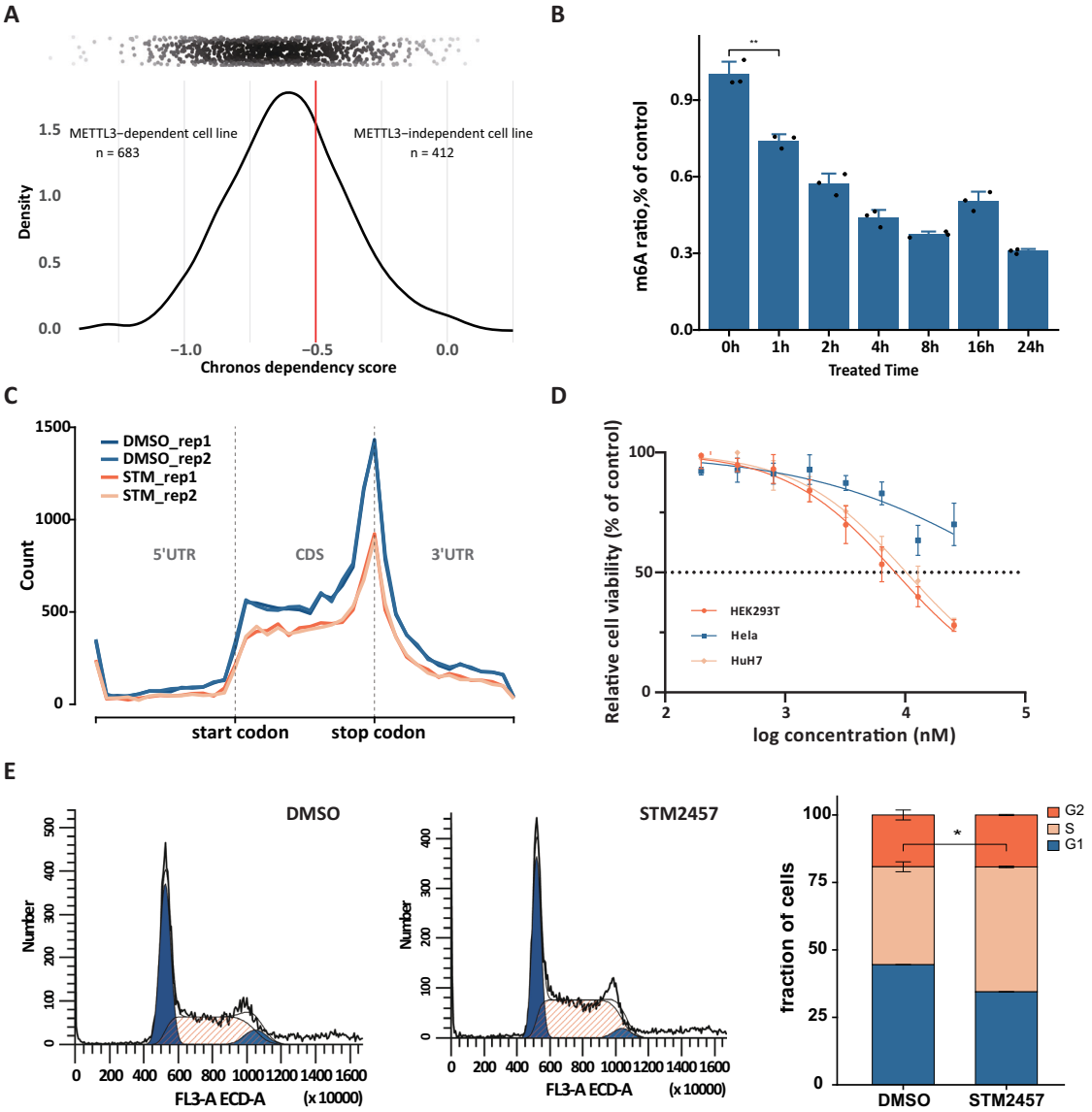

Fig. 1 | m^{6}A modification is essential for cell proliferation. A Distribution of METTL3 dependency scores across 1054 cell lines from the DepMap dataset. The density plot shows the overall distribution of dependency probability scores, where each dot represents an individual cell line. **B** LC-MS/MS analyses of mRNA m^{6}A levels in HEK293T cells treated with 5 μM STM2457 for indicated time. $^{**}p < 0.001$ (two-tailed t test). **C** Metagene plot of the transcriptome-wide m^{6}A distribution of HEK293T cell line treated with STM2457 or DMSO. UTR, untranslated region. **D** Relative cell viability of HEK293T, HuH7, and HeLa cells following STM2457 treatment for 72 h at noted concentration. **E** Cell cycle analysis of HEK293T cells following STM2457 or DMSO treatment for 72 h.

the well-characterized model that m^{6}A negatively regulates gene expression (Fig. 2D).

Given the established role of YTHDF2 in m^{6}A-mediated RNA degradation, we analyzed YTHDF2 CLIP data. Among the 55 upregulated genes with YTHDF2 binding sites. TIGAR (TP53-induced glycolysis and apoptosis regulator), a known regulator of glycolysis and the PPP, was particularly notable (Fig. 2E). Building on this discovery, we conducted a transcription inhibition assay using actinomycin D (ActD), revealing that STM2457 treatment significantly increased the stability of *TIGAR* mRNA (Fig. 2F). To further validate the functional role of *TIGAR* in m^{6}A-mediated regulation of cell proliferation, we performed knockout experiment and confirmed the downregulation efficiency of *TIGAR* mRNA using RT-qPCR (Supplementary Fig. 3A). In HuH7 and HEK293T cells where METTL3 knockdown led to increased *TIGAR* expression (Supplementary Fig. 3B), downregulation of TIGAR rescued the proliferation defect caused by METTL3 knockdown (Supplementary Fig. 3C). These results confirm that *TIGAR* is a key mediator of the anti-proliferative effects of m^{6}A reduction.

m^{6}A deficiency drives metabolic reprogramming

The well-characterized function of *TIGAR* in glycolysis prompt us to further explore the metabolic consequences of m^{6}A deficiency. We conducted targeted metabolomics assay, focusing on the pathway of glucose metabolism. The clustering analysis effectively segregated the control group from the treatment group, highlighting the rewiring of glucose metabolism following STM2457 treatment (Fig. 3A). Intriguingly, cellular metabolites in m^{6}A-deficient samples generally exhibited a decline, with a notable decrease in glucose-6-phosphate (G6P) levels representing reduced glucose utilization. Specifically, pronounced suppression of certain metabolites was observed, particularly glycolytic intermediates such as Phosphoenolpyruvate, D-Fructose 1,6-bisphosphate and NADP (Fig. 3A). Given the pivotal role of NADP in the pentose phosphate pathway (PPP), its reduced levels often indicate increased activity within the PPP[27]. To directly confirm the shift in metabolic flux, we performed ^{13}C-labeled glucose tracing experiments in HuH7 and HEK293T cells following METTL3

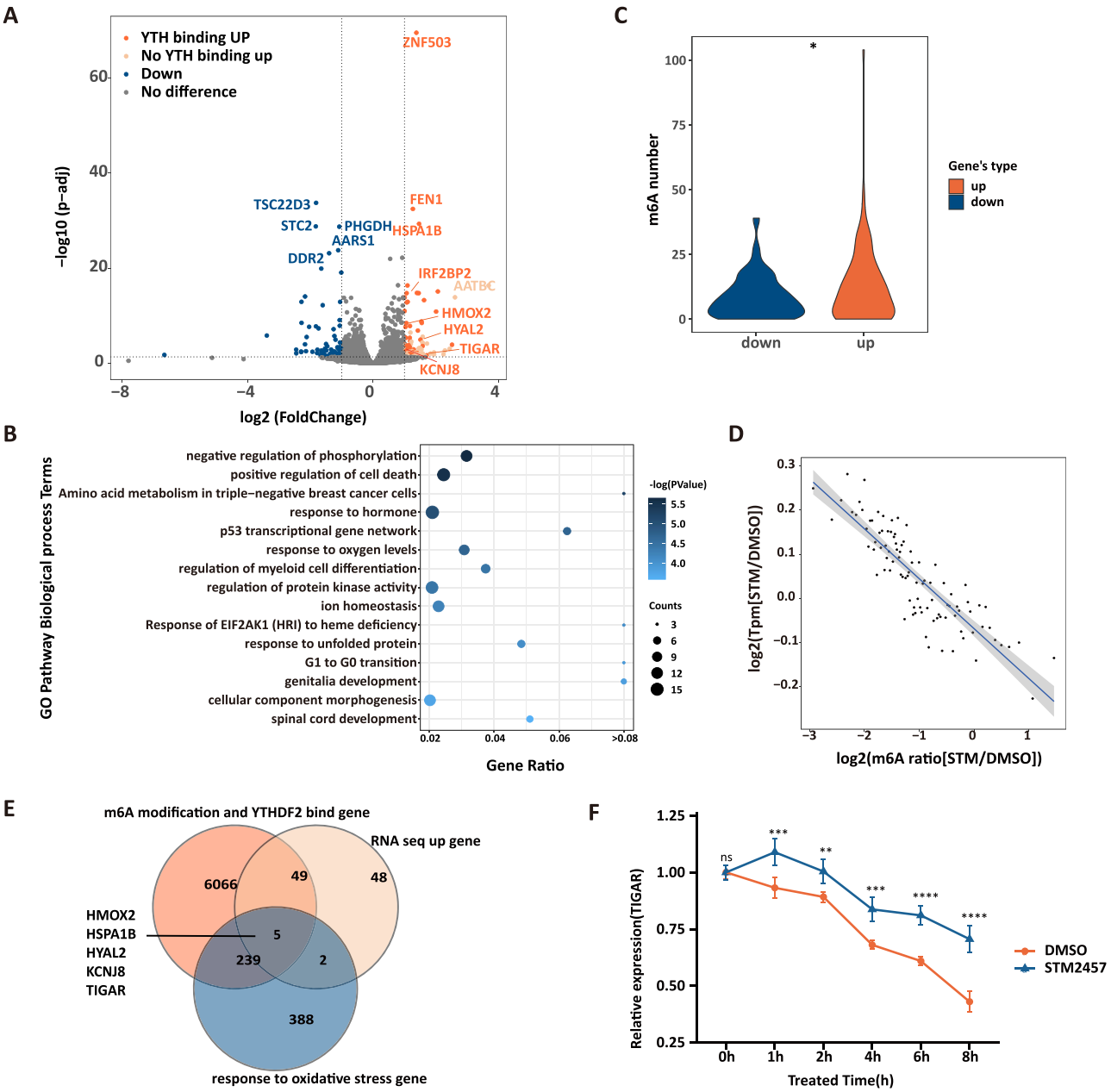

Fig. 2 | *TIGAR* is a key mediator of the anti-proliferative effects of m^{6}A reduction. **A** Volcano plot of the differentially expressed genes between STM2457-treated and control cells across two biological replicates. Upregulated genes with YTHDF2 binding sites are highlighted. **B** Gene Ontology analysis of differentially expressed genes under STM2457 treatment. Statistical test was determined by one-sided hypergeometric test. **C** The number of m^{6}A modification sites in genes that are upregulated and downregulated under STM2457 treatment. The data of m^{6}A modification sites were obtained from reported articles[40]. **D** The correlation between changes in m^{6}A level and gene expression changes in control or STM2457 treated HEK293T cells. **E** Venn diagram shows substantial and significant overlap among metabolic genes, variated genes in inhibitor treated cells (> 2 folds change), and YTHDF2 binding genes in wild type HEK293T cells. **F***TIGAR* expression in HEK293T cells treated with STM2457 for 24 h and then further treated with Act-D for the indicated times. The mRNA level was measured by RT-qPCR. Data are presented as the mean ± SD from Six independent experiments. *$p < 0.05$, **$p < 0.01$, by two-tailed t test.

knockdown. These experiments revealed a significant increase of ^{13}C incorporation into lactate in both cell lines (Fig. 3B), confirming enhanced PPP activity upon m^{6}A reduction. These findings demonstrate that m^{6}A modification, through its regulation of TIGAR, plays a crucial role in balancing glycolysis and the PPP.

CRISPR screen identifies G6PD as a key regulator of m^{6}A-dependent cell proliferation

To identify genes whose knockout modulates the cell growth suppression caused by low m^{6}A, we performed a genome-wide CRISPR-Cas9 screen. We introduced a sgRNA library targeting 18,360 protein-encoding genes (each gene targeted by 4 distinct sgRNAs) into HEK293T cells constitutively expressing Cas9. After two weeks of culture with or without STM2457, we used NGS to uncover the variation of sgRNA representation (Fig. 4A). Gini index was calculated to ensure the equal distribution of sgRNA in both the treated and control groups (Supplementary Fig. 4A). Enrichment of specific sgRNAs indicates that deletion of the corresponding genes could affect the proliferation arrest induced by reduced m^{6}A.

We next used the MAGeCK method to rank genes based on their effect on cell growth in the low-m^{6}A environment, where genes with elevated

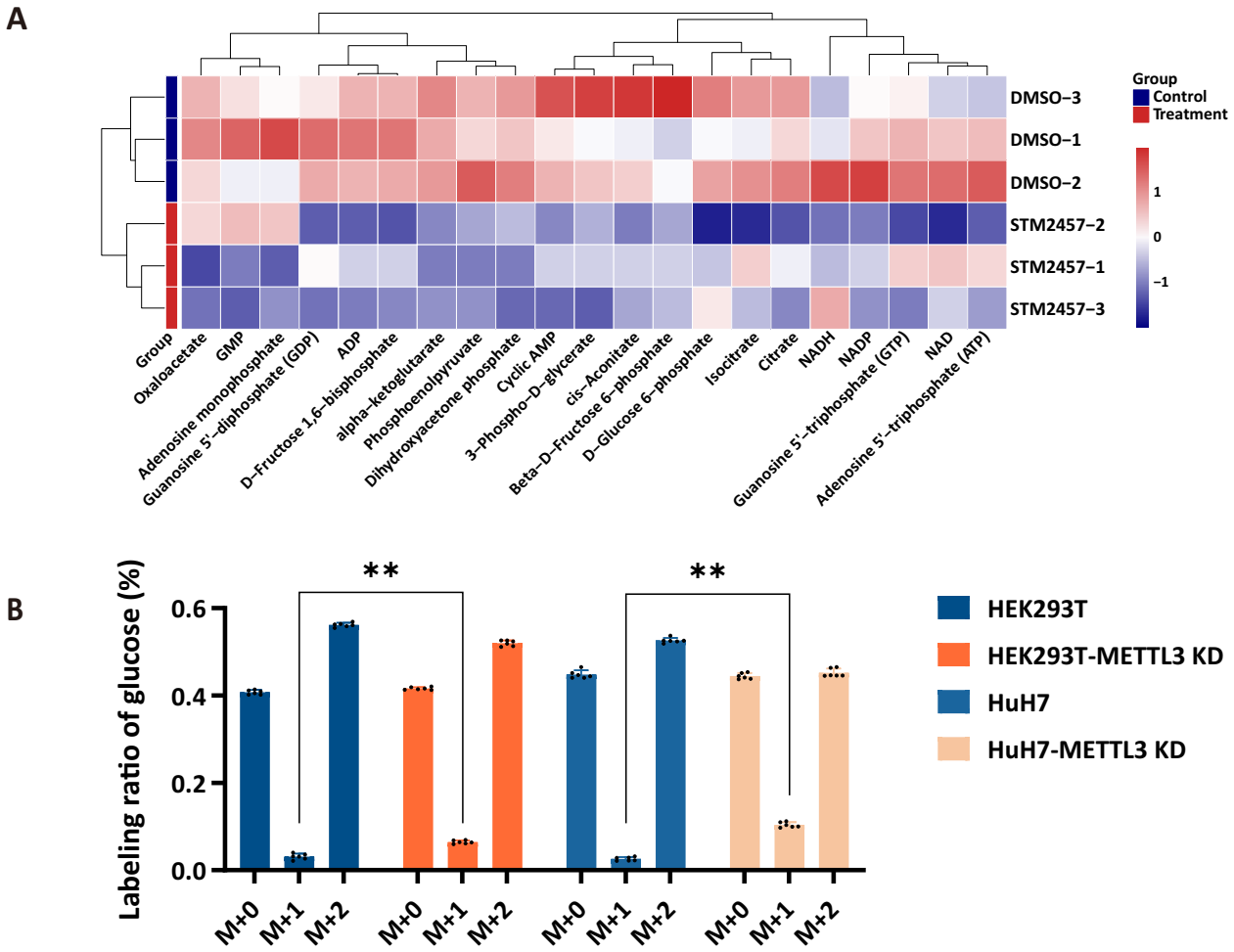

Fig. 3 | m^{6}A deficiency shifts glucose metabolism from glycolysis to the pentose phosphate pathway. A Heatmap showing changes in metabolite levels in HEK293T cells treated with STM2457 compared to DMSO-treated control cells. **B** Isotopic tracing analysis of the pentose phosphate pathway in HuH7 and HEK293T cells following *METTL3* knockdown. Cells were cultured in medium containing ^{13}C-glucose. The relative abundance of different isotopologues of lactate (M + 0, M + 1, and M + 2) is shown.

scores correspond to accelerated cell growth upon gene knockout, and lower scores represent further proliferation arrest. GO enrichment analysis of these candidate genes revealed biological processes associated with RNA processing, such as splicing, mRNA methylation, and transcription elongation (Fig. 4B). Notably, knockout of core m^{6}A methyltransferase complex components (e.g., METTL14, RBM15, ZC3H13, WTAP) further impaired proliferation (Fig. 4C), confirming the importance of m^{6}A in cell growth. The top 50 genes with positive scores exhibited enrichment in metabolic process functionalities such as cellular metabolic process and cellular biosynthetic process (Fig. 4D). For precision, we identified genes whose knockout significantly affected proliferation in low-m^{6}A conditions (FDR < 0.05) (Fig. 4E, Supplementary Fig. 4B). ZC3H13 emerged as a strong negative selection mark (knockout further impairs proliferation), while HNRNPA1 and G6PD emerged as positive selection marks (knockout rescues the proliferation defect) (Fig. 4E).

To validate these findings, we used dual sgRNAs targeting selected genes, including two negative selection mark genes (*ZC3H13* and *JTB1*) and three positive selection mark genes (*G6PD*, *STARD7*, and *FAM193A*). PCR amplification of editing sites followed by NGS sequencing confirmed the editing efficiency (Supplementary Fig. 4C). Additionally, Western Blot and RT-qPCR results confirmed a significant reduction in targeted protein to a very low level (Supplementary Fig. 4D, E). Consistent with the whole-genome screen, knockout of *ZC3H13* and *JTB* impaired proliferation in STM2457-treated cells, while knockout of *G6PD*, *STARD7*, and *FAM193A* enhanced proliferation (Fig. 4F). We further validated G6PD's role by performing knockout and overexpression experiments in HEK293T and HuH7 cells with METTL3 knockdown. (Supplementary Fig. 4F). These experiments confirmed that G6PD modulates proliferation in the context of low m^{6}A, regardless of whether m^{6}A reduction is achieved by STM2457 treatment or METTL3 knockdown.

m^{6}A deficiency induces S phase arrest through ROS-dependent CDK2 inactivation

To further investigate the mechanism by which m^{6}A regulates cell proliferation, we focused on G6PD, whose knockout rescued the proliferation defect in the CRISPR screen. G6PD has been reported to reversely regulate m^{6}A level[28]. To test this, we employed LC-MS/MS to measure m^{6}A methylation levels in HEK293T cells post G6PD suppression. However, our data showed no discernible change in m^{6}A levels compared to controls, suggesting alternative explanation for the observed cellular phenotype (Fig. 5A). Given the enrichment of metabolic genes in the screen (Fig. 4D), we hypothesized that G6PD might exert its effects through modulating glucose metabolism. Specifically, STM2457 treatment led to a notable decrease in intracellular ROS levels (Fig. 5B), suggesting an interplay between m^{6}A and redox homeostasis. Since G6PD is the rate-limiting enzyme in the PPP, which generates NADPH, we reasoned that G6PD knockdown would affect ROS levels. Indeed, suppressing G6PD, which would limit NADPH production through the PPP, reversed the decrease in

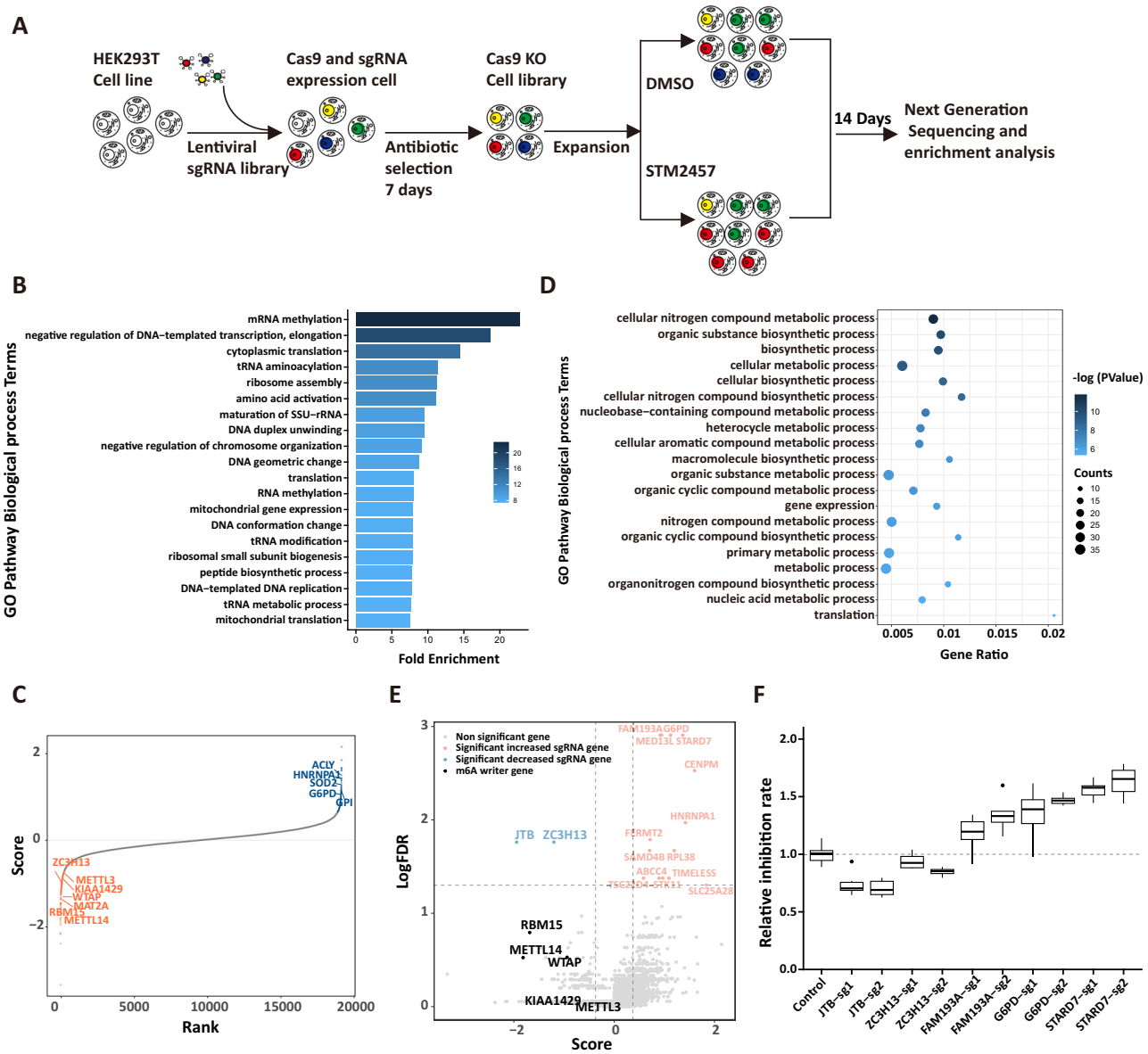

Fig. 4 | Genome-wide CRISPR screen identifies genetic effectors of cellular sensitivity to m^{6}A modification. A Schematic workflow of the genome-wide CRISPR-Cas9 screen. HEK293T cells expressing Cas9 were transduced with a lentiviral sgRNA library targeting 18,360 protein-coding genes. Cells were then treated with STM2457 or DMSO for 14 days. Genomic DNA was extracted, and sgRNA representation was determined by next-generation sequencing (NGS). Enrichment analysis was performed to identify genes whose knockout affected cell proliferation in the presence of STM2457. **B** Gene Ontology (GO) analysis of the top 200 genes enriched from the STM2457 treated cell screen presented in (**C**). **C** Scatter plot showing gene rankings based on their MAGeCK scores from the CRISPR screen with STM2457 treatment. **D** GO enrichment analysis of the top 50 positively selected genes (i.e., genes whose knockout rescued the anti-proliferative effect of STM2457). **E** Scatterplot depicting gene level results for METTL3 inhibitor selected hits in the CRISPR screen. A number of representative hits are shown in color. **F** Validation of candidate genes from the CRISPR screen. Relative cell proliferation of cells with knockout of the indicated genes and treated with STM2457 for 72 h. Data are presented as mean ± SD of three independent experiments.

ROS caused by STM2457 (Fig. 5B). Furthermore, STM2457 treatment increased NADPH levels by ~30%, and this increase was reversed by G6PD suppression (Fig. 5C).

ROS serves as both byproduct of mitochondrial processes and a signaling agent affecting diverse cellular functions such as cell proliferation[29]. Given the observed decrease in ROS and the S-phase arrest following STM2457 treatment (Fig. 5D), we next investigated the role of CDK2, a key regulator of S phase progression whose activity is controlled by phosphorylation at Tyr15 and Thr160 (T160)[30]. While STM2457 treatment did not alter CDK2 protein levels, it significantly decreased phosphorylation at T160 (Fig. 5E, Supplementary Fig. 5). Suppressing G6PD, which restored ROS levels, also restored CDK2 T160 phosphorylation (Fig. 5E, Supplementary Fig. 5) and reversed the S-phase arrest (Fig. 5D). These findings demonstrate that m^{6}A modification, influences glucose metabolism through its regulation of TIGAR, leading to decreased ROS levels. This decrease in ROS, in turn, reduces CDK2 T160 phosphorylation and induces S phase arrest, ultimately impairing cell proliferation (Fig. 5F).

G6PD is involved in m^{6}A regulated cancer progression

Given the critical role of m^{6}A in cell proliferation and our finding that G6PD modulates this process, we investigated the clinical relevance of *G6PD* and *METTL3* expression in cancer. Focusing on liver hepatocellular carcinoma (LIHC), we analyzed gene expression and survival data from the TCGA database. As expected, *METTL3* was upregulated in LIHC tumors (Fig. 6A), and high *METTL3* expression correlated with poorer prognosis (Fig. 6B). Further analysis revealed a positive

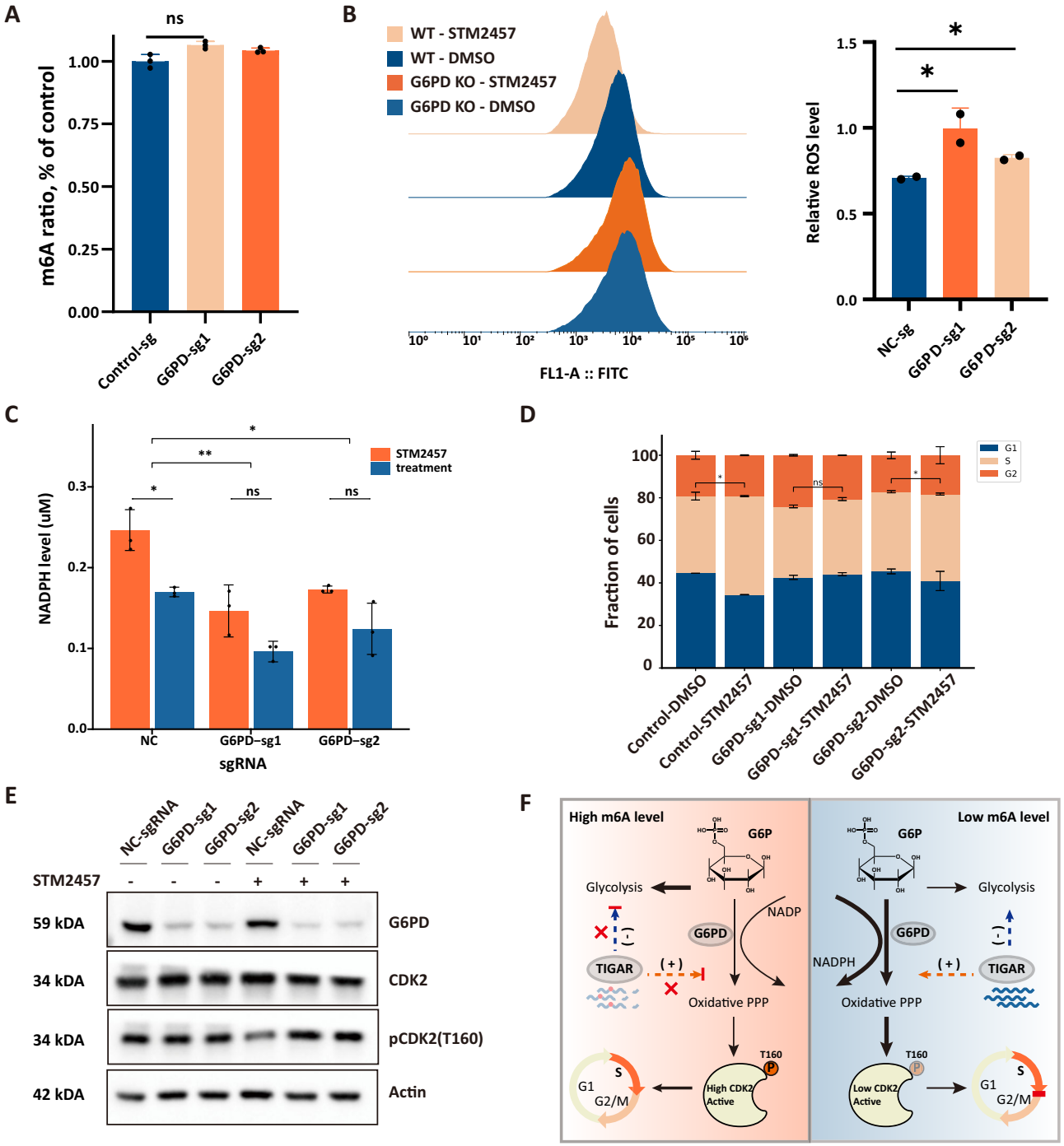

Fig. 5 | m^{6}A modification regulates S phase arrest. A Relative m^{6}A levels of control and G6PD KO cells. $p < 0.05$ is considered statistically significant. $^{**}p < 0.01$ (two-tailed t test [**A**, **B**]). **B** Intracellular ROS levels. Left: Scatter plot depicting the measurement of ROS in cells treated with DMSO and STM2457 in a representative experiment. Right: Relative ROS level of *G6PD* KO and control cell lines. The numerical values on the vertical axis represent the ratio between the STM2457-treated group and the control group. **C** NADPH levels in cells with or without *G6PD* knockout, cells treated with STM2457 for 24 h. Data are presented as the mean ± SD from three independent experiments. $^{*}p < 0.05$, $^{**}p < 0.01$ (two-tailed t test [**C**, **D**]). **D** Cell cycle analysis of *G6PD* KO and control cell lines treated by STM2457 for 72 h. Data are presented as the mean ± SD from three independent experiments. **E** Western blot analysis of indicated proteins in cells treated with DMSO or STM2457 to confirm CDK2 and CDK2(T160) protein level. **F** Schematic model depicting the mechanism by which m^{6}A modification regulates cell proliferation via TIGAR, glucose metabolism, ROS, CDK2, and cell cycle progression.

correlation between *METTL3* and *G6PD* expression in LIHC (Fig. 6C), indicating a potential functional link between these two genes. Interestingly, patients with low expression of both *METTL3* and *G6PD* had a poorer prognosis than those with low *METTL3* and high *G6PD* (Fig. 6D), consistent with our findings in cell proliferation models.

This observation raised the intriguing possibility that activation of G6PD could enhance the efficacy of METTL3 inhibitor and further suppress tumor cell proliferation. To test this, we treated HEK293T cells with the m^{6}A inhibitor STM2457 in combination with AG1, a potent and selective G6PD activator. Intriguingly, treatment with AG1 significantly

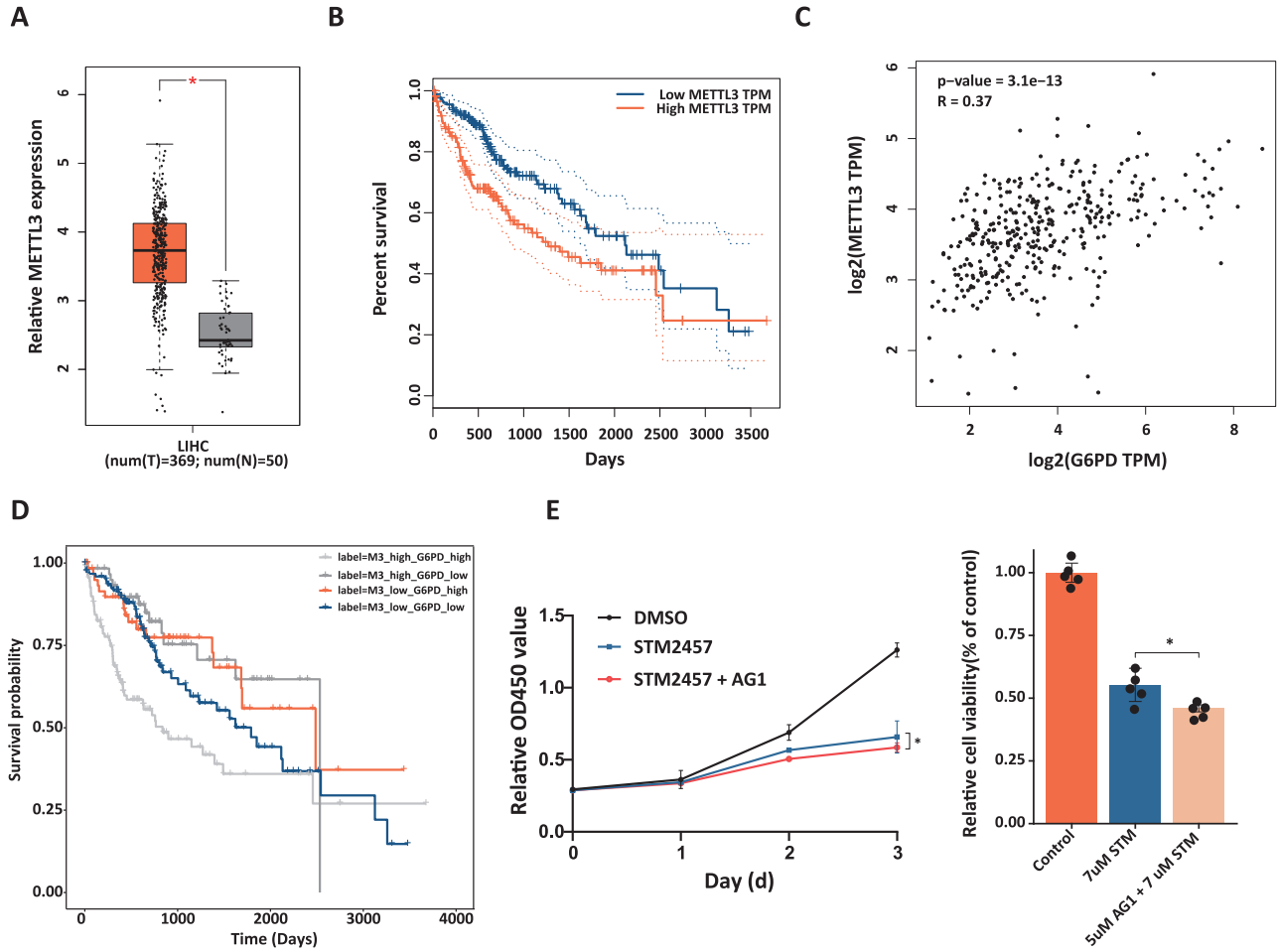

Fig. 6 | *G6PD* is involved in m^{6}A regulated LIHC progression. A Relative *METTL3* expression in LIHC samples from TCGA database compared to normal tissue. **B** Kaplan-Meier survival curves for LIHC patients stratified by METTL3 expression (high vs. low). **C** Pearson correlation analysis of the correlation between *G6PD* and *METTL3* in LIHC. **D** Combine analysis of the prognosis of LIHC with different expression of *METTL3* and *G6PD* by KM curve. **E** Effect of G6PD activation on the anti-proliferative activity of STM2457. Left: Growth curves of HEK293T cells treated with STM2457 alone or in combination with the G6PD activator AG1. Right: Relative cell viability of HEK293T cells treated with STM2457 alone or in combination with AG1 for 72 h. *$p < 0.05$ (two-tailed t-test).

enhanced the growth inhibitory effect of STM2457, reducing proliferation by an additional 15% (Fig. 6E). These results suggest that LIHC patients with low *METTL3* and high *G6PD* expression may be particularly sensitive to METTL3 inhibitors, highlighting the potential of combining METTL3 inhibition with G6PD activation could be a viable therapeutic strategy.

Discussion

Several studies have highlighted the impact of m^{6}A on cell proliferation, making the knockout of *METTL3* challenging in most cell lines. Consequently, the facile and efficient construction of a low methylation cell model is of great importance for elucidating the biological functions of m^{6}A. In this study, we systematically investigated the effects of STM2457 on m^{6}A levels in various cell lines and species. Our findings revealed that this inhibitor effectively reduced intracellular m^{6}A levels, with the decrease in m^{6}A levels positively correlating with both the duration and concentration of drug treatment. These results underscore the efficacy of STM2457 in constructing a low m^{6}A methylation cell model and emphasize the importance of m^{6}A in cell proliferation.

Our low m^{6}A methylation cell model revealed a strong inverse correlation between m^{6}A modification and gene expression, and genes with augmented expression possessed a greater number of m^{6}A modification sites. These results coincide with the YTHDF2-mediated RNA destabilizing effects. Through an integrative analysis of RNA-seq data, MeRIP-seq data, and YTHDF2 binding sites data, we identified six genes that are actively responsive to decreased m6A modification. Among these genes, TIGAR emerged as particularly significant due to its role in regulating glucose metabolism[31]. Our results indicate that m^{6}A modification on TIGAR mRNA can regulate its decay, which appears to be dynamic in response to stimuli and stress. These findings highlight the roles of m^{6}A in the dynamic balance of different glucose metabolism pathways in cancer cells.

It is widely recognized that the PPP plays a critical role in cancer cell growth, however, our data suggest a more nuanced scenario. While STM2457 treatment indeed enhances PPP activity, we propose that the consequent shift in metabolic flux from glycolysis to PPP is not sufficient to support the proliferative demands of cancer cells[32–36]. This shift may disrupt the metabolic homeostasis required for sustained cancer cell proliferation, thereby leading to growth inhibition. This interpretation is supported by evidence that the glycolytic flux, rather than PPP activity, is the predominant factor driving cancer cell growth in the contexts studied[37,38]. Additionally, our findings are consistent with reports that G6PD deficiency, a key enzyme in the PPP, does not affect the growth and progression of certain tumors, and that alternative metabolic pathways can compensate for G6PD deficiency in tumor cells[39]. This perspective emphasizes the context-dependent nature of PPP's role in cancer cell metabolism and proliferation. It also underscores the importance of understanding the metabolic plasticity of cancer cells and how therapeutic interventions, such as m6A modification, can exploit this plasticity to inhibit cell growth.

To gain deeper insights into the function of m^{6}A in regulating cell proliferation, we employed loss-of-function CRISPR screens to profile genetic interactions within a low m^{6}A modification cellular environment in human HEK293T cells. This screening approach successfully uncovered central genes closely associated with m^{6}A modification, including the key component genes of m^{6}A writer and RNA splicing-related genes. Notably, we also identified previously uncharacterized genes whose deletion resulted in variations in cell proliferation, thereby expanding our understanding of m^{6}A modification regulation. Among these newly identified regulators, the G6PD module emerged as a notable candidate gene most vulnerable to m^{6}A level. Although previous studies have indicated that inhibiting *G6PD* with siRNA can increase mRNA m^{6}A levels in 3T3-L1 cells[40], our data did not support. This discrepancy may be attributed to differences in our approach to reducing G6PD; specifically, we used CRISPR Cas9 to knock out the *G6PD* gene instead of using siRNA. In addition to *G6PD*, our screening highlighted other metabolism-regulating genes such as *STARD7*, *STK11*, and *SLC25A28* as negative regulators in response to low m^{6}A conditions. While we did not delve further into how these genes impact cell proliferation in low m^{6}A conditions, our CRISPR screen results provide valuable insights, enhancing our understanding of how m^{6}A influences cell phenotypes.

Cells must orchestrate cell growth driven by metabolism alongside precise cell cycle progression to ensure the duplication of DNA and other essential cellular components before cell division. As, Reactive oxygen species (ROS), which are by-products of mitochondrial respiration, also serve as signaling molecules affecting various cellular processes[41]. Previous studies have demonstrated the integration of ROS signals into cell cycle control through a direct interaction with cyclin-dependent kinase 2 (CDK2)[30]. In our present study, we uncover the involvement of m^{6}A modification in regulating these processes. We confirmed that low m^{6}A modification can increase the pentose phosphate pathway (PPP) through the upregulation of *TIGAR* gene expression, thereby leading to a reduction in cellular ROS levels. This reduction in ROS levels causes CDK2 deactivation, ultimately resulting in S phase arrest. Notably, our results establish a connection between post-transcriptional m^{6}A modification and cell cycle progression through glucose metabolism. Furthermore, other studies have shown that m^{6}A modification of cell-cycle-specific cyclin mRNA can undergo periodic changes during the cell cycle[42,43]. Both of these effects essentially involve m^{6}A modification regulating gene expression through mRNA stability. The direct and indirect regulatory mechanisms on cell cycle regulation underscore the complexity of m^{6}A modification function. In summary, our results affirm the involvement of m^{6}A modification in glucose metabolism, consequently affecting cell cycle progression. These findings underscore the significance of epitranscriptomic regulation in glucose metabolism pathways and reveal the susceptibility of cell proliferation to m^{6}A modification.

Materials and methods

Cell culturing

HEK293T, Hela, HuH7, NR, C2C12 and DF1 cell lines were cultured in 10% (v/v) FBS (Excell Bio, FSP500) containing DMEM medium (Corning, 10-013) at 37 °C under 5% CO2 and showed negative in regulate mycoplasma contamination testing. S2 cell lines were cultured in 10% (v/v) FBS containing Schneider's Drosophila Medium (Gibco) at 25 °C.

Compounds

STM2457 (MCE #HY-134836), Actinomycin D (MCE, HY-17559) and puromycin (MCE, HY-B1743A) were obtained from MedChemexpress company. Drugs for in vitro studies were dissolved in DMSO (Sigma, D2650) to yield 5 mM stock solutions and stored at 20 °C.

LC-MS/MS for detection and quantification of RNA modifications

RNA modifications of m^{6}A were detected according to a previously published procedure[33]. To analyze the content of RNA modifications in cellular mRNA, 200 ng extracted rRNA-depleted RNA from cells was digested into nucleosides by Nuclease P1 (1 U, NEB, M0660S) and shrimp alkaline phosphatase (rSAP, 1 U, NEB, M0371S) in 50 µl RNase-free water at 37 °C overnight. The mixture was diluted to 100 µl, 10 µl of which was injected into an LC-MS/MS system consisting of a high-performance liquid chromatographer (Shimadzu) equipped with a C18-T column (Weltech) and a Triple Quad 4500 (AB SCIEX) mass spectrometer in positive ion mode by multiple-reaction monitoring. Mass transitions of m/z 268.0–136.0 (A), m/z 245.0–113.1 (U), m/z 244.0–112.1 (C), m/z 284.0–152.0 (G), m/z 282.0–150.1 (m1A), m/z 282.0–150.1 (m^{6}A) and m/z 258.1–126.1 (m5C) were monitored and recorded. A concentration series of pure commercial nucleosides (MCE) was employed to generate standard curves. Concentrations of nucleosides in samples were obtained by fitting signal intensities to standard curves with certain ratios calculated subsequently[44].

Multiple sequence alignment

Protein sequences were downloaded from the Uniprot database (https://www.uniprot.org/), while nucleotide sequences were obtained from the Ensembl database (https://www.ensembl.org/index.html). Alignment was performed using CLUSTALW with default parameters, in the respective protein or DNA mode. Finally, the alignment results were visualized using ESPript (https://espript.ibcp.fr/ESPript/cgi-bin/ESPript.cgi).

Short-term cell proliferation assay

Cells were seeded in 96-well microplates (Corning, 3599) at a density of 1000 cells in 100 ml of complete cell culture medium per well and allowed to adhere overnight. Cells were treated in sextuple with 100 ul serial dilutions of compound in complete cell culture medium (final DMSO concentration = 0.1%). Following drug exposure for 72 h, 10 ul of Cell counting Kit-8 (DOJINDO, CK04) per well was added and plates were incubated at 37 °C for 2 h. Luminescence was read in a Multi-Mode Microplate Reader (SpectraMax i3x). Assay data were normalized to DMSO values and plotted using a four-parameter concentration-response model in GraphPad Prism 7. The figures show the mean ± standard deviation of sextuple values from representative experiments.

RNA-seq and data analysis

RNA libraries were constructed by NEBNext® Ultra II Directional RNA Library Prep Kit for Illumina (NEB, E7760S/L) according to the manufacturer's instructions. Libraries were quality assessed and quantified using the BioAnalyzer 2100 system (Agilent Technologies, Inc., USA). Library sequencing was performed on an illumina NovaSeq 6000 instrument with 150 bp paired end reads. Next, we used Cutadapt (v2.6) to trim adapter sequences and subsequently performed quality control with FastQC (v0.11.9). The cleaned reads were then aligned to the hg38 (Ensemble GRCh38 v100) reference genome using HISAT2 (v2.1.0)[45]. Read counts mapped to genes were quantified with FeatureCounts (v1.6.0)[46]. For differential expression analysis, we used DESeq2, setting selection criteria for differentially expressed genes at an FDR < 0.05 and an absolute log2Fold change value > 1[47]. Finally, GO enrichment analysis of these genes was executed using the clusterProfiler package[48].

MERIP-seq and data analysis

RNA modifications of m^{6}A were detected according to a previously published procedure[49]. Briefly, Nonribosomal RNA samples were first fragmented to 150 nt by Fragmentation Reagent (Thermo Fisher, AM8047), and then the purified fragmented RNA was end-repaired using T4 Polynucleotide Kinase (Thermo Fisher, EK0031). These sample were then ligated to adenylated (NEB, E2610) barcoded 3′ adapters using T4 RNA ligase 2, truncated KQ (NEB, M0373). The excess adapters were subsequently removed by Lambda Exonuclease (NEB, M0262). Protein G (Thermo Fisher, 10004D) beads were coupled to the m^{6}A antibody (CST, 56593) by rotating at room temperature for 1 h. The RNA fragments were incubated with the bead-linked antibodies and rotated at 4 °C for 2 h. The bound RNA was washed with buffer twice, then eluted from the beads with buffer RLT (QIAGEN, 79216). IP and Input samples were ligated with 5'

adapters using T4 RNA ligase1 (NEB, M0204). First Strand cDNA for IP and Input samples were Synthesis using HiScript III 1st Strand cDNA Synthesis Kit (Vazyme, R312), and the library amplification was performed using 2 × KAPA HiFi Hot Start Ready Mix (KAPA Biosystems, #KK2602 7958935001). The cleaned reads were then aligned to the hg38 (Ensemble GRCh38 v100) reference genome using HISAT2 (v2.1.0).Read counts mapped to genes were quantified with FeatureCounts (v1.6.0). M^6A enriched region were detected by MACS2 software[50]. For differential expression analysis, we used DESeq2.

Targeted mass spectrometry

Collect 5×10^6 cell samples and flash freeze them with liquid nitrogen, then lyophilize using a freeze-dryer. Subsequently, add 100ul of water and 400 ul of methanol-acetonitrile solution (1:1, v/v). Add 10 ul of the internal standard, vortex for 60 s, and sonicate at a low temperature for 30 min. Allow it to sit at −20 °C for 1 h to precipitate the proteins. Then, centrifuge at 14,000 rcf and 4 °C for 20 min. Collect the supernatant, freeze-dry, and store the samples at −80 °C. For separation, the samples were analyzed using the Agilent 1290 Infinity LC ultra-high performance liquid chromatography system. The samples were placed in an autosampler at 4 °C, with a column temperature of 35 °C. The mobile phase A consists of a 50 mM ammonium acetate aqueous solution + 1.2% ammonium hydroxide, while the mobile phase B is a 1% acetone in acetonitrile solution, flowing at 300 μL/min with an injection volume of 2 μL. The liquid phase gradient is as follows: 0–1 min, 70% B; 1–10 min, B linearly changes from 70% to 60%; 10-12 min, B linearly changes from 60% to 30%; 12.1–15 min, B remains at 30%; 15–15.5 min, B linearly changes from 30% to 70%, and 15.6–22 min, B stays at 70%. In the sample queue, a QC sample is set at intervals for detecting and evaluating the stability and repeatability of the system; in the sample queue, a mixture of standard substances of the target substance is set for the correction of the chromatographic retention time. Mass spectrometry analysis was performed using the 5500 QTRAP mass spectrometer (SCIEX) in negative ion mode. The conditions for the 5500 QTRAP ESI source are as follows: source temperature 450 °C, Ion Source Gas1 (Gas1): 45, Ion Source Gas2 (Gas2): 45, Curtain gas (CUR): 30, ionSapary Voltage Floating (ISVF) −4500 V. The MRM mode was used to detect the ions to be tested, and the ion pair information of all target substances can be found in Attachment 1. The chromatographic peak area and retention time were extracted using the Multiquant 3.0.2 software. The metabolites were identified by calibrating the retention time with the standards of the target substances.

RNA lifetime measurement by qPCR

Stability of RNA in DMSO and STM2457 treated HEK293T cells was achieved by incubating cells with actinomycin D (Act-D, Sigma, A9415) at 5 μg/ml. Cells were then collected at the indicated times and RNA was isolated for Real-time PCR. Half-life (t1/2) of TIGAR mRNA was calculated using ln2/ slope and 18S rRNA was used for normalization.

Cell cycle assay

The cell cycle profile of samples were measured using a Cell Cycle and Apoptosis Analysis kit (Beyotime, C1052). Cells (1×10^5 cell/ml, 2 ml) were seeded in a six-well plate. After treatment, the cells were fixed in ice-cold 70% ethanol at 4 °C overnight. Then the cells were incubated at 37 °C for 30 min with propidium working solution containing 10 μl of RNase A. Samples were analyzed using a CytoFlex flow cytometer (Beckman Coulter, Brea CA) at excitation/emission of 488/575 nm, and 5000 cells were collected per sample. Data were analyzed using the FlowJO 10.81 software.

Genome-wide sgRNA library amplification and packaging

Human Brunello CRISPR knockout pooled library was a gift from David Root and John Doench (Addgene, 73178)[51]. The plasmid library was amplified and validated as described in the Broad GPP protocol. Validation to check gRNA presence and representation was performed using calc_auc_v1.1.py (https://github.com/mhegde/) and count_spacers.py[52].

Library packaging was performed as described previously[52]. The sgRNA libraries were packaged into lentiviral particles using HEK293T cells. For each cell dish, 5.5 million cells were transfected 24 h after plating using 60 ul Lipofectamine™ 2000 Transfection Reagent (Thermo Fisher Scientific, 11668027) diluted in 1.5 ml Opti-MEM (Gibco, 11058021) that was combined with 12 ug of the sgRNA library, 4 ug of pMD2.G (Addgene plasmid, 12259) and 8 ug of psPAX2 plasmid (Addgene plasmid, 12260). The next day, the transfected cells received fresh medium. 48 hr post-transfection, lentivirus was collected, filtered, aliquoted, and frozen at 80 °C. Viral titer was determined using the Lenti-X qRT-PCR Titration Kit (Clontech, 631235) and was typically in the range of 5×10^6 transforming units/ml.

Genome-wide CRISPR-Cas9 screen

A total of 1.4×10^8 HEK293T cells were distributed across 40 of the 10 cm^2 tissue culture dishes (3.5×10^6 cells per dish) and infected with the Brunello library of lentiviral particles at an MOI of 0.3 in 10 ml of complete DMEM (DMEM supplemented with 10% fetal bovine serum (Excell Bio, FSP500) supplemented with 8 ug/ml polybrene (Sigma, TR-1003-G) and incubated for 24 h for efficient transduction. 24 h after infection, the culture medium was replaced with fresh medium containing 1 mg/ml puromycin. These transduced cells were expanded with intermittent passaging to avoid overcrowding of the cells and to generate a sufficient number of cells for the downstream whole-genome CRISPR-KO screens. An adequate number of cells were used as a control to obtain a representation (screen depth) of > 500 cells for each sgRNA of the library, and a similar number of cells were treated with vehicle control (DMSO) or the STM2457(MCE, HY-134836) at 7 uM final concentration for 14 days. The vehicle-treated control cell population and the surviving cells from the STM2457 treated samples were subjected to CRISPR screen enrichment analysis. The total genomic DNA (gDNA) was isolated using FastPure® Blood/Cell/Tissue/Bacteria DNA Isolation Mini Kit (Vazyme, DC112) and the concentrations of gDNA were measured using Equalbit 1 × dsDNA HS Assay Kit (Vazyme, EQ121-01). The MAGeCK pipeline was used to robustly estimate the $\log_2$fold change (FC) and significance of the enriched gRNA/genes from the cell death-based CRISPR screens[53].

Generation of candidate gene KO cell lines

HEK293T cell lines with constitutive Cas9 expression were generated by lentiviral infection and antibiotic selection. Cas9 expression was confirmed by immunoblotting and gene editing efficiency was tested as follows. Cas9-expressing cells were infected at a low (~0.5) multiplicity of infection (MOI) with lentivirus expressing either a control sgRNA or sgRNA targeting candidate genes and then selected with puromycin. Cells were subsequently seeded in 6-well tissue culture plates. Cell culture medium was exchanged 3 days later and the experiment was terminated at day 7. Genomic DNA of sgRNA target was subjected to PCR analysis by using Phusion High-Fidelity DNA Polymerase. The PCR products were performed on an illumina NovaSeq 6000 instrument with 150 bp paired end reads.

Intracellular ROS determination

Total intracellular ROS was determined by staining cells with dichlorofluorescin diacetate (Beyotime, S0033S). Briefly, cells (5×10^4 cells/ml, 100 μl/well) were seeded in a 96-well black plate. After treatment, cells were incubated with 10 μM DCFH-DA probe at 37 °C for 20 min. Then cells were washed twice with PBS. The fluorescence was read with a fluorescence microplate reader at excitation/emission of 535/610 nm. The fluorescence images were obtained with Multi-Mode Microplate Reader (SpectraMax i3x).

NADPH quantification assay

The HEK293T cells or G6PD KO cells were plated in six-well plates at 1×10^6 cell/well. Cells were treated with or without STM2457 for the

designated time. Then, 200 μL NADP + / NADPH extraction solution (Beyotime, S0179) and the extracts were centrifuged at 12000 g for 8 min at 4 °C to collect the supernatant. The supernatant (50 μL) was added to the 96 well plates together with G6PDH working solution and incubated at 37 °C for 10 min. Then the absorbance was read at 450 nm absorbance.

Western blot

Samples were homogenized in RIPA buffer (Beyotime #P0013D) containing 1 × protease inhibitor cocktail and 1 × phosphatase inhibitor cocktail (Sigma #P5726). Lysates were boiled with 4× loading buffer (Beyotime, P0015) at 95 °C for 10 min, then centrifuged at 13,000 rpm at 4 °C for 10 minutes. The samples were subsequently stored at −80 °C for future use. A total of 30 μg protein per sample was loaded into 10% SimplePAGE Bis-Tris gel (Sangon Biotech, C691101) and transferred to PVDF membranes (Abcam, ab133411). Membranes were blocked in 5% milk TBST for 1 h at room temperature (RT), incubated in a diluted primary antibody solution at 4 °C overnight, washed and incubated in a dilution of secondary antibody conjugated to HRP for 1 h at RT. Protein bands were detected using SuperSignal West Dura Extended Duration Substrate kit (Thermo) and FluroChem R (Proteinsimple).

Reporting summary

Further information on research design is available in the Nature Portfolio Reporting Summary linked to this article.

Data availability

Sequencing data generated in this work can be found in GEO with the accession number GSE261509. The source data behind the graphs in the paper can be found in Supplementary Data.

Received: 15 March 2024; Accepted: 14 March 2025;
Published online: 26 March 2025

References

1. Shi, H., Wei, J. & He, C. J. M. C. Where, when, and how: context-dependent functions of RNA methylation writers, readers, and erasers. *Mol. Cell* **74**, 640–650 (2019).
2. Roundtree, I. A., Evans, M. E., Pan, T. & He, C. J. C. Dynamic RNA modifications in gene expression regulation. *Cell* **169**, 1187–1200 (2017).
3. Frye, M., Harada, B. T., Behm, M. & He, C. RNA modifications modulate gene expression during development. *Science* **361**, 1346–1349 (2018).
4. Hsu, P. J., Shi, H. & He, C. Epitranscriptomic influences on development and disease. *Genome Biol.* **18**, 197 (2017).
5. Raj, N. et al. The Mettl3 epitranscriptomic writer amplifies p53 stress responses. *Mol. Cell*. (2022).
6. Hou, G. et al. SUMOylation of YTHDF2 promotes mRNA degradation and cancer progression by increasing its binding affinity with m6A-modified mRNAs. *Nucleic Acids Res* **49**, 2859–2877 (2021).
7. Barbieri, I. et al. Promoter-bound METTL3 maintains myeloid leukaemia by m(6)A-dependent translation control. *Nature* **552**, 126–131 (2017).
8. Lin, S., Choe, J., Du, P., Triboulet, R. & Gregory, R. I. The m6A Methyltransferase METTL3 Promotes Translation in Human Cancer Cells. *Mol. Cell* **62**, 335–345 (2016).
9. Choe, J. et al. mRNA circularization by METTL3-eIF3h enhances translation and promotes oncogenesis. *Nature* **561**, 556–560 (2018).
10. Yankova, E. et al. Small-molecule inhibition of METTL3 as a strategy against myeloid leukaemia. *Nature* **593**, 597–601 (2021).
11. Pavlova, N. N., Zhu, J. & Thompson, C. B. The hallmarks of cancer metabolism: Still emerging. *Cell Metab.* **34**, 355–377 (2022).
12. Warburg, O. On the Origin of Cancer Cells. *Science* **123**, 309–314 (1956).
13. Lin, X., Xiao, Z., Chen, T., Liang, S. H. & Guo, H. Glucose Metabolism on Tumor Plasticity, Diagnosis, and Treatment. *Front. Oncol.* **10**, (2020).
14. Colegio, O. R. et al. Functional polarization of tumour-associated macrophages by tumour-derived lactic acid. *Nature* **513**, 559–563 (2014).
15. Sullivan, H. C. et al. Triple-negative breast carcinoma in African American and caucasian women: Clinicopathology, immunomarkers, and outcome. *Appl. Immunohistochemistry Mol. Morphol.* **22**, 17–23 (2014).
16. TeSlaa, T., Ralser, M., Fan, J. & Rabinowitz, J. D. The pentose phosphate pathway in health and disease. *Nat. Metab.* **5**, 1275–1289 (2023).
17. Jen, K. Y. & Cheung, V. G. Identification of novel p53 target genes in ionizing radiation response. *Cancer Res* **65**, 7666–7673 (2005).
18. Bensaad, K. et al. TIGAR, a p53-inducible regulator of glycolysis and apoptosis. *Cell* **126**, 107–120 (2006).
19. Le, X. et al. DNA methylation downregulated ZDHHC1 suppresses tumor growth by altering cellular metabolism and inducing oxidative/ER stress-mediated apoptosis and pyroptosis. *Theranostics* **10**, 9495 (2020).
20. Reid, M. A., Dai, Z. & Locasale, J. W. The impact of cellular metabolism on chromatin dynamics and epigenetics. *Nat. Cell Biol.* **19**, 1298–1306 (2017).
21. Huang, X. et al. LINC00842 inactivates transcription co-regulator PGC-1α to promote pancreatic cancer malignancy through metabolic remodelling. *Nat. Commun.* **12**, 3830 (2021).
22. Zhang, C. et al. Reduced m6A modification predicts malignant phenotypes and augmented Wnt/PI3K-Akt signaling in gastric cancer. *Cancer Med* **8**, 4766–4781 (2019).
23. Zhang, H. et al. m(6)A methyltransferase METTL3 promotes retinoblastoma progression via PI3K/AKT/mTOR pathway. *J. Cell Mol. Med* **24**, 12368–12378 (2020).
24. Li, Z. et al. N6-methyladenosine regulates glycolysis of cancer cells through PDK4. *Nat. Commun.* **11**, 2578 (2020).
25. Wang, Y. et al. LncRNA LINRIS stabilizes IGF2BP2 and promotes the aerobic glycolysis in colorectal cancer. *Mol. Cancer* **18**, 174 (2019).
26. Poh, H. X., Mirza, A. H., Pickering, B. F. & Jaffrey, S. R. Alternative splicing of METTL3 explains apparently METTL3-independent m6A modifications in mRNA. *PLoS Biol.* **20**, e3001683 (2022).
27. Wrigley, N. G., Heather, J. V., Bonsignore, A. & Flora, A. D. Human erythrocyte glucose 6-phosphate dehydrogenase: Electron microscope studies on structure and interconversion of tetramers, dimers and monomers. *J. Mol. Biol.* **68**, 483–499 (1972).
28. Wang, L. et al. NADP modulates RNA m6A methylation and adipogenesis via enhancing FTO activity. *Nat. Chem. Biol.* **16**, 1394–1402 (2020).
29. Armstrong, L. et al. Human induced pluripotent stem cell lines show stress defense mechanisms and mitochondrial regulation similar to those of human embryonic stem cells. *Stem Cells* **28**, 661–673 (2010).
30. Kirova, D. G. et al. A ROS-dependent mechanism promotes CDK2 phosphorylation to drive progression through S phase. *Developmental Cell* **57**, 1712–1727.e1719 (2022).
31. Mor, I., Cheung, E. C. & Vousden, K. H. Control of glycolysis through regulation of PFK1: old friends and recent additions. *Cold Spring Harb. Symp. Quant. Biol.* **76**, 211–216 (2011).
32. Ge, T. et al. The Role of the Pentose Phosphate Pathway in Diabetes and Cancer. *Front Endocrinol. (Lausanne)* **11**, 365 (2020).
33. Wu, S. et al. Transcription Factor YY1 Promotes Cell Proliferation by Directly Activating the Pentose Phosphate Pathway. *Cancer Res* **78**, 4549–4562 (2018).
34. Zhang, X. et al. PAK4 regulates G6PD activity by p53 degradation involving colon cancer cell growth. *Cell Death Dis.* **8**, e2820–e2820 (2017).

35. Nakamura, M. et al. Glucose-6-phosphate dehydrogenase correlates with tumor immune activity and programmed death ligand-1 expression in Merkel cell carcinoma. *J. Immunother. Cancer* **8**, (2020).
36. Ding, H. et al. Activation of the NRF2 antioxidant program sensitizes tumors to G6PD inhibition. *Sci. Adv.* **47**, eabk1023 (2021).
37. Kowalik, M. A. Columbano, A. & Perra, A. Emerging Role of the Pentose Phosphate Pathway in Hepatocellular Carcinoma. *Front. Oncol.* **7**, (2017).
38. Ghergurovich, J. M. et al. Glucose-6-Phosphate Dehydrogenase Is Not Essential for K-Ras-Driven Tumor Growth or Metastasis. *Cancer Res* **18**, 3820–3829 (2020).
39. Chen, L. et al. NADPH production by the oxidative pentose-phosphate pathway supports folate metabolism. *Nat. Metab.* **1**, 404–415 (2019).
40. Liu, C. et al. Absolute quantification of single-base m6A methylation in the mammalian transcriptome using GLORI. *Nat. Biotechnol.* **41**, 355–366 (2023).
41. Ray, P. D., Huang, B. -W. & Tsuji, Y. Reactive oxygen species (ROS) homeostasis and redox regulation in cellular signaling. *Cell. Signal.* **24**, 981–990 (2012).
42. Hirayama, M. et al. FTO Demethylates Cyclin D1 mRNA and Controls Cell-Cycle Progression. *Cell Rep.* **31**, 107464 (2020).
43. Li, H. et al. METTL3 promotes cell cycle progression via m(6)A/YTHDF1-dependent regulation of CDC25B translation. *Int J. Biol. Sci.* **18**, 3223–3236 (2022).
44. Zhang, Z. et al. Single-base mapping of m6A by an antibody-independent method. *Sci. Adv.* **5**, eaax0250 (2019).
45. Kim, D., Langmead, B. & Salzberg, S. L. HISAT: a fast spliced aligner with low memory requirements. *Nat. Methods* **12**, 357–360 (2015).
46. Liao, Y., Smyth, G. K. & Shi, W. featureCounts: an efficient general purpose program for assigning sequence reads to genomic features. *Bioinformatics* **30**, 923–930 (2013).
47. Love, M. I., Huber, W. & Anders, S. Moderated estimation of fold change and dispersion for RNA-seq data with DESeq2. *Genome Biol.* **15**, 550 (2014).
48. Yu, G., Wang, L. G., Han, Y. & He, Q. Y. clusterProfiler: an R package for comparing biological themes among gene clusters. *Omics* **16**, 284–287 (2012).
49. Liu, X. -H. et al. Co-effects of m6A and chromatin accessibility dynamics in the regulation of cardiomyocyte differentiation. *Epigenetics Chromatin* **16**, 32 (2023).
50. Zhang, Y. et al. Model-based Analysis of ChIP-Seq (MACS). *Genome Biol.* **9**, R137 (2008).
51. Doench, J. G. et al. Optimized sgRNA design to maximize activity and minimize off-target effects of CRISPR-Cas9. *Nat. Biotechnol.* **34**, 184–191 (2016).
52. Joung, J. et al. Genome-scale CRISPR-Cas9 knockout and transcriptional activation screening. *Nat. Protoc.* **12**, 828–863 (2017).
53. Li, W. et al. MAGeCK enables robust identification of essential genes from genome-scale CRISPR/Cas9 knockout screens. *Genome Biol.* **15**, 554 (2014).

Acknowledgements

This work was supported by the Ministry of Science and Technology of China (2022YFC3400400, 2022YFA0912900), National Natural Science Foundation of China (32425034, 92253202, 32271499, 32270644, and 32100461), Pearl River Talent Recruitment Program (2019ZT08Y485), and Shenzhen Bay Scholars Program.

Author contributions

G.Z.L. conceived the project; J.F.X. conducted the experiments with the assistance from H.X.C and W.S.C; B.D.L. and G.R.T. analyzed the data with the assistance from Z.H.R., Y.L.L.; J.F.X wrote the manuscript with the assistance from F.Y., Z.L. and Z.Z; S.C.Y., J.K.W., L.C., and G.Z.L. revised the manuscript. All authors reviewed the results and approved the final version of the manuscript.

Competing interests

The authors declare no competing interests.

Additional information

Supplementary information The online version contains supplementary material available at https://doi.org/10.1038/s42003-025-07937-9.

Correspondence and requests for materials should be addressed to Guan-Zheng Luo.

Peer review information *Communications Biology* thanks Zhihao Wang, Kenan Sevinc, Gaofeng Fan and the other, anonymous, reviewer(s) for their contribution to the peer review of this work. Primary Handling Editors: Mengtan Xing and Christina Karlsson Rosenthal. A peer review file is available.